Whereas the CO-to-H I line intensity ratio increases twofold between D39 ($R = 11$ kpc) and the inner arm around D153 ($R = 6$ kpc), the slope of the $I(CO)/\tau_R$ relation remains the same. Yet D153 is not only closer to the centre, but it also shows a much lower star formation activity. Does this mean that Allen and co-workers[8] are wrong? Their contention that there is a large hidden molecular mass rests on two cloud complexes located at 2 kpc from the centre and might apply only to the innermost region. There, the thick stellar bulge prevents the estimation of τ_R. We note, however, that their mass estimates assume viral equilibrium and a smooth CO brightness distribution, two assumptions that do not seem fulfilled in the largest complex, D478. There, CO profiles[8] are broad and double-peaked, and look typical of kinematically perturbed clouds near H I regions (such as D47 in Fig. 2b). They also show evidence of CO brightness fluctuations on scales of 40 pc. Thus, even in these innermost regions, the evidence for hidden molecular gas is meagre.

Because CO is a good tracer of H_2, Fig. 1a yields the molecular cloud distribution in M31 with an unprecedented resolution. The brightest clouds are grouped in narrow filamentary arms, which stand out against a rich background of fainter clouds. The connection of the arm segments into a spiral pattern is not straightforward. One solution is illustrated by the three ellipses of Fig. 1a. It assumes a major axis position angle PA $= 42°$, the value that fits the southern velocity field best, and an inclination on the plane of the sky $i = 78°$. In this picture, all the bright CO clouds lie on three circular arms of radii $R = 7$, 11 and 18 kpc and on the border of the stellar super-association NGC 206. Another arm pattern[17] assumes that PA $= 38°$ and two logarithmic spirals with a pitch angle of 7°.

The CO arms are very narrow, as illustrated in Fig. 2, which shows the cloud complexes associated with D47 and D84, observed with resolution of 2″ (9 pc). The bright blobs of Fig. 1 are now resolved into thin, clumpy filaments quite similar in brightness and size to Orion A and Orion B[18]; the peak CO brightness temperature, averaged over the ~9 pc beam, is 7 K. We note that, although D84 is the strongest CO source in the southwest half of M31, Orion is not the brightest source by far in the Milky Way, but only the brightest in the vicinity of the Sun. Obviously, M31 lacks a bright inner structure like the Galactic 'Molecular Ring', but it shows relatively strong molecular emission up to $R = 18$ kpc, farther than the Milky Way[19].

Does CO emission trace the molecular gas in other galaxies as well as in M31? A correlation between CO arms and dark dust lanes is also observed[11,20] in the Sc-type spiral M51, but on a coarser scale. M51, 10 Mpc away, is the archetype of spirals with a high star-formation rate. Poorer resolution and a less uniform stellar background make it difficult to repeat our analysis, but again, all conspicuous dark lanes of M51 seem to have bright CO counterparts. The millimetre dust emission has been mapped in M51 (ref. 13) and in half a dozen of Sb–Sd spirals, including NGC 891 (ref. 12), which is often considered a twin of the Milky Way. Except in the outermost parts of the disks, there is a tight correlation between this emission and CO. Although the dust emission depends on temperature, this tight correlation strongly suggests that CO is indeed a fair tracer for the molecular clouds in most spiral galaxies. □

Received 9 January; accepted 8 July 1998.

1. Maloney, P. & Black, J. H. Molecular gas abundances in galaxies. *Astrophys. J.* **325,** 389–401 (1988).
2. Stanek, K. Z. & Garnavich, P. M. Distance to M31 with the *HST* and *Hipparcos* Red Clump Stars. *Astrophys. J. Lett.* **503,** L131–L134 (1998).
3. Hodge, P. *The Andromeda Galaxy* Ch. 10–12 (Astrophysics and Space Science Library, Vol. 176, Kluwer, Dordrecht, 1992).
4. Walterbos, R. A. M. & Kennicutt, R. C. Jr An optical study of stars and dust in the Andromeda galaxy. *Astron. Astrophys.* **198,** 61–86 (1988).
5. Brinks, E. & Shane, W. W. A high resolution H I line survey of M 31. *Astron. Astrophys. Suppl.* **55,** 179–251 (1984).
6. Dame, T. M. *et al.* A complete CO survey of M 31. *Astrophys. J.* **418,** 730–742 (1993).
7. Loinard, L. *et al.* Molecular spiral arms in M 31. *Astrophys. J.* **469,** L101–L104 (1996).
8. Loinard, L. & Allen, R. J. Cold massive molecular clouds in the inner disk of M 31. *Astrophys. J.* **499,** 227–233 (1998).
9. Tilanus, R. P. J. & Allen, R. J. Spiral structure of M 83. *Astron. Astrophys.* **274,** 707–729 (1993).
10. Bohlin, R. C., Savage, B. D. & Drake, J. F. A survey of interstellar HI from Lα absorption measurements. *Astrophys. J.* **224,** 132–142 (1978).
11. Rand, R. J., Kulkarni, S. R. & Rice, W. Star formation and the distribution of HI and infrared emission in M 51. *Astrophys. J.* **390,** 66–78 (1992).
12. Guélin, M. *et al.* 1.3 mm emission in the disk of NGC 891: evidence of cold dust. *Astron. Astrophys.* **279,** L37–L40 (1993).
13. Guélin, M. Cold dust emission from the spiral arms of M 51. *Astron. Astrophys.* **298,** L29–L32 (1995).
14. Blair, W. P., Kirshner, R. P. & Chevalier, R. A. Abundance gradients in M 31. *Astrophys. J.* **254,** 50–69 (1982).
15. Walterbos, R. A. M. & Schwering, P. B. W. Infrared emission from interstellar dust in the Andromeda Galaxy. *Astron. Astrophys.* **180,** 27–49 (1987).
16. Strong, A. W. & Mattox, J. R. Gradient model analysis of EGRET diffuse Galactic γ-ray emission. *Astron. Astrophys.* **308,** L21–L24 (1996).
17. Braun, R. Distribution and kinematics of neutral gas in M 31. *Astrophys. J.* **372,** 54–66 (1991).
18. Maddalena, R. J. *et al.* The large system of molecular clouds in Orion and Monoceros. *Astrophys. J.* **303,** 375–391 (1986).
19. Heyer, M. *et al.* the FCRAO CO survey of the Outer Galaxy. *Astrophys. J. Suppl.* **115,** 241–258 (1998).
20. Garcıa-Burillo, S., Guélin, M. & Cernicharo, J. CO in M 51. I. Molecular spiral structure. *Astron. Astrophys.* **274,** 123–147 (1993).
21. Emerson, D. T. & Gräve, R. The reduction of scanning noise in raster scanned data. *Astron. Astrophys.* **190,** 353–358 (1988).
22. Hoernes, P. Thesis, Univ. Bonn (1997).

Acknowledgements. We thank the IRAM Granada staff, particularly A. Sievers and W. Brunswig, and P. Hoenes from MPIfR for their important role in developing the 'on-the-fly' observation and data-reduction procedures. We also thank E. Brinks and N. Devereux for making available their H I and Hα data.

Correspondence and requests for materials should be addressed to N.N. (e-mail: nneini@astro.uni-bonn.de) and M.G. (e-mail: guelin@iram.fr).

Microwave spectroscopy of a quantum-dot molecule

T. H. Oosterkamp*, T. Fujisawa*†, W. G. van der Wiel*, K. Ishibashi*‡, R. V. Hijman*, S. Tarucha† & L. P. Kouwenhoven*

** Department of Applied Physics and DIMES, Delft University of Technology, PO Box 5046, 2600 GA Delft, The Netherlands*

† NTT Basic Research Laboratories, 3-1, Morinosoto Wakamiya, Atsugi-shi, Kanagawa 243-0198, Japan

‡ Institute of Physical and Chemical Research (RIKEN), 2-1, Hirosawa, Wako, Saitama 351-01, Japan

Quantum dots are small conductive regions in a semiconductor, containing a variable number of electrons (from one to a thousand) that occupy well-defined, discrete quantum states—for which reason they are often referred to as artificial atoms[1]. Connecting them to current and voltage contacts allows the discrete energy spectra to be probed by charge-transport measurements. Two quantum dots can be connected to form an 'artificial molecule'. Depending on the strength of the inter-dot coupling (which supports quantum-mechanical tunnelling of electrons between the dots), the two dots can form 'ionic' (refs 2–6) or 'covalent' bonds. In the former case, the electrons are localized on individual dots, while in the latter, the electrons are delocalized over both dots. The covalent binding leads to bonding and antibonding states, whose energy difference is proportional to the degree of tunnelling. Here we report a transition from ionic bonding to covalent bonding in a quantum-dot 'artificial molecule' that is probed by microwave excitations[5–8]. Our results demonstrate controllable quantum coherence in single-electron devices, an essential requirement for practical applications of quantum-dot circuitry.

When particles are allowed to tunnel back and forth between two quantum systems, the energy states of the individual systems mix and form new states that extend over both systems. The extended states are referred to as the bonding or symmetric state, and the antibonding or antisymmetric state. In solid-state systems, the energy splitting between bonding and antibonding states have been observed in quantum-well structures[9,10], superconducting tunnelling devices[11,12], and exciton systems[13].

Quantum dots are uniquely engineered solid-state systems in the

sense that they have discrete states and the electrons on the dots are strongly interacting. The question whether different dots can be coupled together in a quantum-mechanically coherent way is non-trivial. The reason is that quantum dots composing single-electron devices are embedded in an environment with many electronic degrees of freedom. The electron that occupies the covalent state of a double-dot system has a Coulomb interaction with all the other electrons confined on the dots and also with the electrons in the current and voltage leads. These interactions can lead to dephasing of the quantum-mechanical wavefunction resulting in a breakdown of the covalent state. For realistic devices there is yet no theory that can calculate reliable dephasing rates. Nevertheless, if elements like quantum dots are ever to be integrated in little quantum circuits[14–16], it is necessary that dots can be coupled coherently.

We have used microwave spectroscopy (0–50 GHz) to measure the energy differences between states in the two dots of the device[2] shown in Fig. 1a. We show that these energy differences, including the bonding–antibonding splitting, is controlled by gate voltages which tune the tunnel coupling between the dots. We first discuss the weak-coupling regime.

Electrons are strongly localized on the individual dots when tunnelling between the two dots is weak. Electron transport is then governed by single-electron charging effects[8]. The charging energies can be tuned away by means of the gate voltages. It is then energetically allowed for an electron to tunnel between dots when a discrete state in the left dot is aligned with a discrete state in the right dot. External voltages also control the alignment of the discrete states. A current can flow when electrons can tunnel, while conserving energy, from the left lead, through the left and right dots, to the right lead. We note that energy is also conserved when a photon of energy hf (where h is Planck's constant), which matches the energy difference between the states of the two dots, is absorbed from the microwave field of frequency f (Fig. 1b).

The resonance in the lowest trace in Fig. 1c is due to an alignment of discrete states. The other traces are measured while applying a microwave signal. The satellite resonances are due to photon-assisted tunnelling processes which involve the emission (left satellite) or absorption (right satellite) of a microwave photon.

Stoof and Nazarov[17] give a detailed description of photon-assisted tunnelling in a double quantum dot. The basic idea is that electrons can absorb fixed quanta of energy hf from a classical oscillating field. An a.c. voltage drop $V = V_{ac}\cos(2\pi ft)$ across a tunnel barrier modifies the tunnel rate through the barrier as[18]:

$$\tilde{\Gamma}(E) = \sum_{n=-\infty}^{+\infty} J_n^2(\alpha)\Gamma(E + nhf) \qquad (1)$$

Here $\tilde{\Gamma}(E)$ and $\Gamma(E)$ are the tunnel rates at energy E with and without an a.c. voltage, respectively; $J_n^2(\alpha)$ is the square of the nth

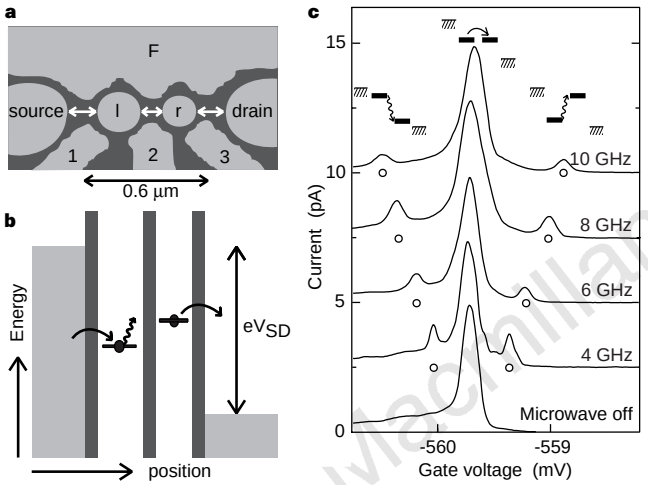

Figure 1 Photon resonances in a double-dot sample. **a**, Photograph of the double quantum dot sample. The source and drain regions as well as the left and right dots are indicated schematically. The tunnel barriers are depicted as arrows. The metallic gates (1, 2, 3 and F) are fabricated on top of a GaAs/AlGaAs heterostructure with a two-dimensional electron gas (2DEG) 100 nm below the surface. At 4.2 K the 2DEG mobility is 2.3×10^6 cm^2 V^{-1} s^{-1} and the electron density is 1.9×10^{15} m^{-2}. Applying negative voltages to all the gates depletes the electron gas underneath them and forms two dots with estimate sizes of 170 nm × 170 nm and 130 nm × 130 nm. We measure the d.c. photocurrent in response to a microwave signal (0–50 GHz) that is capacitatively coupled to gate 2. The tunnel coupling between the two dots and to the reservoirs can be controlled with the voltages on gate 1, 2 and 3. The dots left and right contain about 60 and 35 electrons, respectively. The sample is cooled in a dilution refrigerator, yielding an electron temperature in the source and drain contacts of ~100 mK. **b**, Diagram of the electron energies in the dot for the case that an electron needs to absorb a photon in order to contribute to the current. Shaded areas represent the electron states in the leads that are continuously filled up to the Fermi levels. A voltage V_{SD} applied between the source and drain contacts shifts one Fermi level relative to the other. The discrete energy states in the two dots can be adjusted independently by changing the gate voltages. **c**, The upper diagrams illustrate three situations of the energy state in the left dot relative to the state in the right dot. The hatched lines denote the Fermi levels in the leads. The bottom curve shows the current as a function of the voltage on gate 1 for $V_{SD} = 500\,\mu$V without applying microwaves. A single resonance occurs when two states line up. Other curves, which have been offset for clarity, show the current when microwaves with frequency f from 4 to 10 GHz are applied. Now, two additional satellite resonances occur when the two states are exactly a photon energy apart. The corresponding photon-assisted tunnelling processes are illustrated in the upper diagrams.

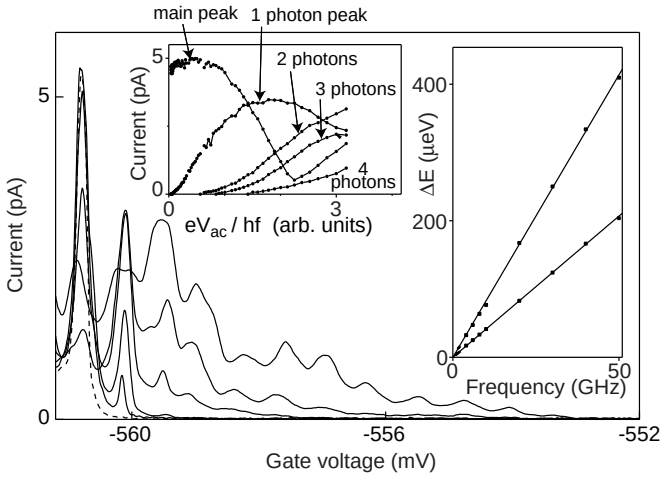

Figure 2 Current versus gate voltage of a weakly coupled double-dot. The dashed curve is without microwaves and contains only the main resonance. The solid curves are taken at 8 GHz for increasing microwave powers resulting in an increasing number of satellite peaks. At the right side of the main peak these correspond to photon absorption. The source–drain voltage $V_{SD} = 700\,\mu$V and the photon energy $hf = 32\,\mu$eV at 8 GHz. At the highest power we observe 11 satellite peaks, demonstrating multiple photon absorption. Left inset, height of the first four satellite peaks as a function of the microwave amplitude. The observed height dependence agrees with the expected Bessel function behaviour. Right inset, distance between main resonance and first two satellites as a function of the applied frequency from 1 to 50 GHz. The distance is transferred to energy through $\Delta E = \kappa \Delta V_g$ where κ is the appropriate capacitance ratio for our device that converts gate voltage V_g to energy[8]. The agreement between data points and the two solid lines, which have slopes of h and $2h$, demonstrates that we observe the expected linear frequency dependence of the one- and two-photon processes.

order Bessel function evaluated at $\alpha = (eV_{ac})/(hf)$, which describes the probability that an electron absorbs or emits n photons of energy hf. e is the electron charge.

Figure 2 shows the current for several microwave powers. The dashed curve shows the main resonance measured at zero power. As the power is increased, satellite peaks appear corresponding to the absorption of multiple photons which are observed up to $n = 11$. At these high powers, the microwaves strongly perturb tunnelling. This is reflected by the nonlinear dependence of the peak heights on power (left inset of Fig. 2), which is in agreement with the expected Bessel-function behaviour.

The right inset to Fig. 2 shows that the separation of the satellite peaks from the main peak depends linearly on frequency between 1 and 50 GHz. As we discuss below, this linearity implies that the tunnel coupling is negligible. The electrons are thus localized on the individual dots and they have an ionic bonding. The line proportional to $2hf$ is taken from data at higher microwave powers where electrons absorb or emit two photons during tunnelling.

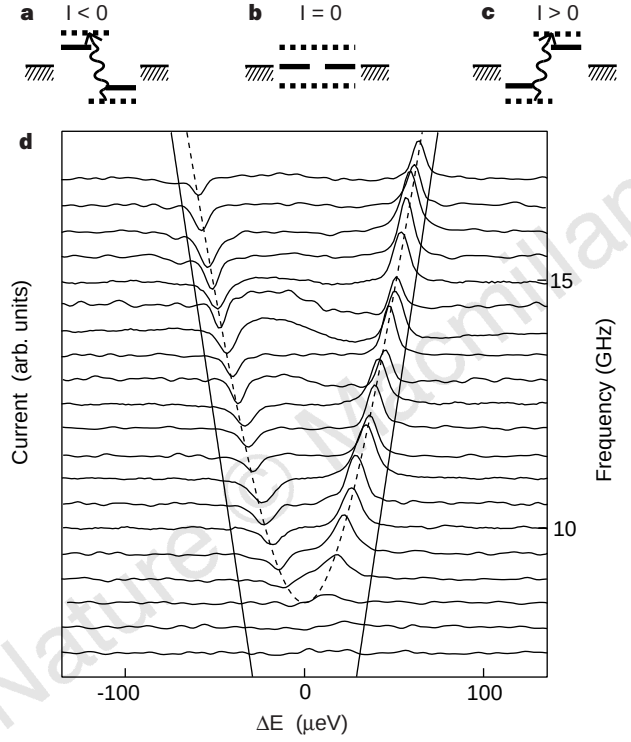

Figure 3 Measured pumped current through the strongly coupled double-dot. **a–c**, Energy diagrams. Solid lines depict the energy states E_{left} and E_{right} in the two dots for the case that the coupling is weak and that their energy difference is simply $\Delta E = E_{left} - E_{right}$. When the dots are strongly coupled, the states delocalize over both dots thereby forming a bonding and an antibonding state. These are indicated by two dotted lines. Their energy difference is $\Delta E^* = [\Delta E^2 + (2T)^2]^{1/2}$. Electrons are transferred from the bonding to the antibonding state when $\Delta E^* = hf$. In **a**, $E_{left} > E_{right}$ which results in electron pumping from right to left corresponding to a negative current. In **b**, the whole system is symmetric ($E_{left} = E_{right}$) and consequently the net electron flow must be zero. In **c**, $E_{left} > E_{right}$ which gives rise to pumping from left to right and a positive current. **d**, Measured pumped current through the strongly coupled double-dot. Gates 1 and 3 are swept simultaneously in such a way that we vary the energy difference ΔE. The different traces are taken at different microwave frequencies, and are offset such that the right vertical axis gives the frequency. The main resonance is absent as we have set $V_{SD} = 0$. The satellite peaks typically have an amplitude of 0.5 pA. For weakly coupled dots the satellite peaks are expected to move linearly with frequency, thereby following the straight solid lines. In contrast, we observe that the satellite peaks follow the fitted dotted hyperbola $hf = [\Delta E^2 + (2T)^2]^{1/2}$ using T as a fitting parameter.

In contrast to the case of weakly coupled dots, covalent bonding occurs when two discrete states that are spatially separated become strongly coupled. Electrons then tunnel quickly back and forth between the dots. In a quantum-mechanical description this results in a bonding and antibonding state which are respectively lower and higher in energy than the original states. Our strong-coupling measurements were made on a second type of double-dot sample (see inset to Fig. 4). To single out the current only due to microwaves we operate the device as an electron pump driven by photons in a way described theoretically by Stafford and Wingreen[19] and by Brune *et al.*[20] (see the diagrams of Fig. 3a–c). By sweeping the gate voltages we vary $\Delta E = E_{left} - E_{right}$, where E_{left} and E_{right} are the energies of the uncoupled states in the left and right dot. The bonding and antibonding states, that are a superposition of the wavefunctions corresponding to an electron in the left or in the right dot, have an energy splitting of $\Delta E^* = E_{antibond} - E_{bond} = [(\Delta E)^2 + (2T)^2]^{1/2}$, where T is the tunnel coupling between the two dots. When the sample is irradiated, a photocurrent may result as illustrated in Fig. 3a–c. A non-zero current indicates that an electron was excited from the bonding state to the antibonding state, thereby fulfilling the condition $hf = \Delta E^*$, or conversely:

$$\Delta E = \sqrt{(hf)^2 - (2T)^2} \qquad (2)$$

Figure 3 shows measured current traces as a function of the uncoupled energy splitting ΔE, where from top to bottom the

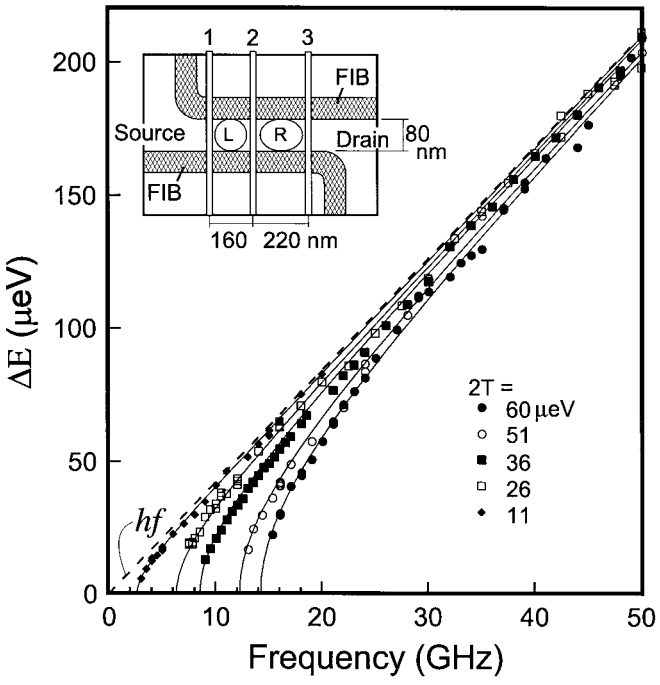

Figure 4 Half the spacing in gate voltage between the positive and negative satellite peaks as a function of frequency. Gate voltage spacing has been transferred to energy difference ΔE (see also Fig. 2 legend). Different curves correspond to different coupling constants T. Solid lines are theoretical fits to $\Delta E = [(hf)^2 - (2T)^2]^{1/2}$. The resulting values for $2T$ are given in the figure. In the limit of weak coupling, this reduces to $\Delta E = hf$ which is indicated by the dashed line. The coupling is varied by applying different voltages to the centre gate (2) or by changing the magnetic field (filled diamonds, $B = 3.3$ T; filled squares, $B = 2.2$ T; other curves, $B = 0$). The upper left inset shows a diagram of the sample[5]. A narrow channel is defined by locally depleting the 2DEG using focused ion beam implantation (FIB). Two dots are then formed by applying negative voltages to the three gates (1, 2, 3) that cross the channel. Microwaves are capacitively coupled to gate 2.

applied microwave frequency is decreased from 17 to 7.5 GHz in 0.5 GHz steps. The distance between the pumping peaks, which is proportional to $2\Delta E$, decreases as the frequency is lowered. However, the peak distance decreases faster than linearly with frequency; the peaks follow the hyperbola rather than the straight lines. The distance goes to zero when the frequency approaches the minimum energy gap between bonding and antibonding states, $hf = 2T$. For frequencies smaller than the coupling, $hf < 2T$, the photon energy is too small to induce a transition from the bonding to the antibonding state.

The coupling between the dots can be decreased by changing the gate voltage on the centre gate to more negative values, or by applying a magnetic field perpendicular to the sample. In Fig. 4 we have plotted the frequency dependence of the energy spacing ΔE at which the pumping current is at a maximum. Different plotting symbols correspond to different centre gate voltage settings and magnetic fields. The solid lines are fits of equation (2) to the measured data. It follows that the coupling $2T$ has been tuned from 11 to 60 μeV. The good agreement with equation (2) and the clear nonlinear frequency dependence demonstrates the control over the formation of covalent bonding between the two dots.

Quantum dots have been suggested as possible candidates for building a quantum computer[14–16]. We have shown that it is indeed possible to coherently couple dots, and that one can induce transitions between the extended states. The next crucial step towards quantum logic gates is to show that the coherence of the superposition is preserved on timescales much longer than the time needed for manipulating the electron wavefunctions. A lower bound for the dephasing time is 1 ns, which we deduce from our narrowest peaks and from the smallest energy gaps between the bonding and antibonding states that we have resolved. We intend to perform measurements of the decoherence time in which the states are manipulated by applying the microwaves in short pulses. □

Received 15 April; accepted 15 July 1998.

1. Ashoori, R. Electrons in artificial atoms. *Nature* **379,** 413–419 (1996).
2. van der Vaart, N. C. *et al.* Resonant tunneling through two discrete energy states. *Phys. Rev. Lett.* **74,** 4702–4705 (1995).
3. Livermore, C. *et al.* The Coulomb blockade in coupled quantum dots. *Science* **274,** 1332–1335 (1996).
4. Blick, R. *et al.* Single electron tunneling through a double quantum dot: The artificial molecule. *Phys. Rev. B* **53,** 7899–7902 (1996).
5. Fujisawa, T. & Tarucha, S. Photon assisted tunneling in single and coupled quantum dot systems. *Superlatt. Microstruct.* **21,** 247–254 (1997).
6. Fujisawa, T. & Tarucha, S. Multiple photon assisted tunneling between two coupled quantum dots. *Jpn J. Appl. Phys.* **36,** 4000–4003 (1997).
7. Oosterkamp, T. H. *et al.* Photon sidebands of the ground state and first excited state of a quantum dot. *Phys. Rev. Lett.* **78,** 1536–1539 (1997).
8. Kouwenhoven, L. P. *et al.* in *Mesoscopic Electron Transport* (eds Sohn, L. *et al.*) 105–214 (NATO ASI Ser. E Vol. 345, 1997); also ⟨http://vortex.tn.tudelft.nl/~leok/papers⟩.
9. Leo, K. *et al.* Coherent oscillations of a wave packet in a semiconductor double-quantum well structure. *Phys. Rev. Lett.* **66,** 201–204 (1991).
10. Mendez, E. E. & Bastard, G. Wannier-Stark ladders and Bloch oscillations in superlattices. *Phys. Today* **46,** 34–42 (1993).
11. Flees, D. J. *et al.* Interband transitions and band gap measurements in Block transistors. *Phys. Rev. Lett.* **78,** 4817–4820 (1997).
12. Nakamura, Y. *et al.* Spectroscopy of energy-level splitting between two macroscopic quantum states of charge coherently superposed by Josephson coupling. *Phys. Rev. Lett.* **79,** 2328–2331 (1997).
13. Schedelbeck, G. *et al.* Coupled quantum dots fabricated by cleaved edge overgrowth: From artificial atoms to molecules. *Science* **278,** 1792–1795 (1997).
14. Landauer, R. Minimal energy requirements in communication. *Science* **272,** 1914–1918 (1996).
15. Barenco, A. *et al.* Conditional quantum dynamics and logic gates. *Phys. Rev. Lett.* **74,** 4083–4086 (1995).
16. Loss, D. & DiVincenzo, D. P. Quantum computation with quantum dots. *Phys. Rev. A* **57,** 120–126 (1998).
17. Stoof, T. H. & Nazarov, Yu. V. Time-dependent resonant tunneling via two discrete states. *Phys. Rev. B* **53,** 1050–1053 (1996).
18. Tien, P. K. & Gordon, J. R. Multiphoton process observed in the interaction of microwave fields with the tunneling between superconductor films. *Phys. Rev.* **129,** 647–651 (1963).
19. Stafford, C. A. & Wingreen, N. S. Resonant photon-assisted tunneling through a double quantum dot: An electron pump from spatial Rabi oscillations. *Phys. Rev. Lett.* **76,** 1916–1919 (1996).
20. Brune, Ph. *et al.* Photon-assisted transport through a double quantum dot with a time-dependent interdot barrier. *Physica E* **1,** 216–218 (1997).

Acknowledgements. We thank R. Aguado, S. M. Cronenwett, S. F. Godijn, P. Hadley, C. J. P. M. Harmans, K. K. Likharev, J. E. Mooij, Yu. V. Nazarov, R. M. Schouten, T. H. Stoof and N. C. van der Vaart for experimental help and discussions. This work was supported by the Dutch Organization for Research on Matter (FOM) and by the EU via the TMR network. L.P.K. was supported by the Dutch Royal Academy of Arts and Sciences (KNAW).

Correspondence and requests for materials should be addressed to T.H.O. (e-mail: tjerk@qt.tn.tudelft.nl).

Localized vibrational modes in metallic solids

V. Keppens*, D. Mandrus*, B. C. Sales*, B. C. Chakoumakos*, P. Dai*, R. Coldea*, M. B. Maple†, D. A. Gajewski†, E. J. Freeman† & S. Bennington‡

** Solid State Division, Oak Ridge National Laboratory, Oak Ridge, Tennessee 37831, USA*
† Department of Physics and Institute for Pure and Applied Physical Sciences, University of California San Diego, La Jolla, California 92093, USA
‡ ISIS Facility, Rutherford Appleton Laboratory, Chilton, Didcot, Oxfordshire, OX11 0QX, UK

Filled skutterudite antimonides[1,2] are cubic compounds with the formula RM_4Sb_{12}, where R is a rare-earth element (such as La or Ce), and M is a transition metal (for example, Fe or Co). The rare-earth ion is weakly bound in an oversized atomic cage formed by the other atoms. Its presence has been shown to cause a dramatic reduction in the lattice component of the thermal conductivity, while having little effect on the electronic properties[3–5] of the compound. This combination of properties makes filled skutterudites of interest as thermoelectric materials. It has been suggested[4] that localized, incoherent vibrations of the rare-earth ion are responsible for the reduction in thermal conductivity, but no direct evidence for these local vibrational modes exists. Here we report the observation of local modes in La-filled skutterudites, using heat capacity, elastic constant and inelastic neutron scattering measurements. The La atoms show unusual thermodynamic behaviour, characterized by the presence of two low-energy localized modes. Our results suggest that consideration of local modes will play an important role in the design of the next generation of thermoelectric materials.

Localized vibrational modes are uncommon in solids because of the strong interactions that exist between the constituent atoms. When present, local modes are usually associated with weakly bound guest atoms that reside in the voids of an open-structured non-metallic host. In metallic solids, which tend to crystallize in close-packed structures, local modes are exceedingly rare. These low-energy vibrational modes, which are not present in the unfilled parent compound $CoSb_3$, give unambiguous evidence for the 'rattling' behaviour of the rare-earth atom in the

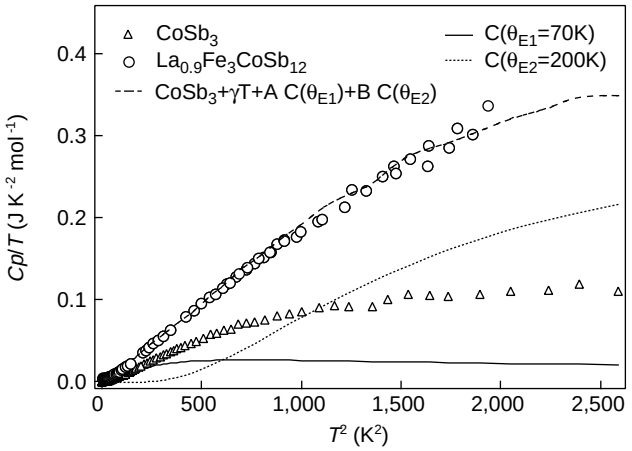

Figure 1 Specific heat divided by temperature versus temperature squared for $La_{0.9}Fe_3CoSb_{12}$ and $CoSb_3$. The dashed line through the $La_{0.9}Fe_3CoSb_{12}$ data is based on a calculation in which the contribution from two Einstein oscillators with level spacings of 70 and 200 K are added to the $CoSb_3$ data (see text for details).